Research Square

Preprints are preliminary reports that have not undergone peer review.
They should not be considered conclusive, used to inform clinical practice,
or referenced by the media as validated information.

Distribution-Level Active Learning for Probabilistic Characterization of Pore Properties in Laser Powder Bed Fusion

Tasrif Ul Anwar
Utah State University
Marcus Noack
Lawrence Berkeley National Laboratory
Nadia Kouraytem
nadia.kouraytem@usu.edu

Utah State University
Maher Alghalayini
malghalayini@lbl.gov

Lawrence Berkeley National Laboratory https://orcid.org/0000-0002-4071-0272

Research Article

Keywords: Additive manufacturing; Laser powder bed fusion; Porosity; Gaussian process regression; Active learning; Uncertainty quantification

Posted Date: November 20th, 2026

DOI: https://doi.org/10.21203/rs.3.rs-11790014/v1

License: This work is licensed under a Creative Commons Attribution 4.0 International License.
Read Full License

Additional Declarations: The authors declare no competing interests.

Distribution-Level Active Learning for Probabilistic Characterization of Pore Properties in Laser Powder Bed Fusion

Tasrif Ul Anwar[1], Marcus M. Noack[2], Nadia Kouraytem[1*], Maher B. Alghalayini[2,3*]

[1]Department of Mechanical and Aerospace Engineering, Utah State University, Old Main Hill, Logan, 84322, Utah, USA.
[2]Applied Mathematics and Computational Research Division, Lawrence Berkeley National Laboratory, Cyclotron Road, Berkeley, 94720, California, USA.
[3]Molecular Foundry, Lawrence Berkeley National Laboratory, Cyclotron Road, Berkeley, 94720, California, USA.

*Corresponding author(s). E-mail(s): nadia.kouraytem@usu.edu; malghalayini@lbl.gov;
Contributing authors: tasrif.anwar@usu.edu; MarcusNoack@lbl.gov;

Abstract

Porosity governs the performance of laser powder bed fusion (LPBF) parts, yet it is usually characterized by scalar summary statistics that discard the variability and multimodality of real pore populations. We present a probabilistic framework that predicts full distributions of pore sphericity and maximum Feret diameter as continuous functions of laser power and scan velocity. The pore population of each 316L specimen, measured by micro-computed tomography, is represented as a four-component lognormal mixture, and multitask Gaussian processes learn how the mixture parameters vary with process settings. The surrogate captures distribution shifts across keyhole, optimal, and lack-of-fusion regimes, confirmed by leave-one-out cross-validation. We also introduce an active-learning acquisition function that targets epistemic uncertainty in the predicted density. In synthetic campaigns, it achieves a given accuracy in fewer experiments than grid and random sampling do for the Wasserstein-1 distance, Kullback–Leibler divergence, and log-predictive density. This offers a general approach to probabilistic pore characterization and efficient experimental design.

Keywords: Laser Powder Bed Fusion; Gaussian Process Regression; Distribution-level Active Learning; Porosity Distribution Characterization

Introduction

Additive Manufacturing (AM), particularly Laser Powder Bed Fusion (LPBF), is transforming the fabrication of complex metallic components, offering unparalleled design freedom and material efficiency, and is especially impactful in high-value sectors such as aerospace, biomedicine, and energy [1, 2]. However, LPBF process parameters critically dictate the resulting microstructure and

the formation of functional defects, most notably porosity, which together govern the mechanical, thermal, electrical, and biological performance of the fabricated component [3–5]. Understanding and controlling porosity is therefore central to optimizing LPBF processes and tailoring porosity toward application-specific requirements. However, achieving this control remains difficult, as fully characterizing the variability in pore size and shape across the high-dimensional processing parameter space is a significant challenge.

Traditional approaches to studying the effects of LPBF process parameters on porosity, typically design-of-experiments frameworks coupled with ex situ microstructural analysis, are inherently resource-intensive and limited in the resolution and extent to which the process space can be explored [6, 7]. As a result, they cannot feasibly capture the full stochastic variability of pore properties across a high-dimensional parameter space, nor efficiently identify the processing windows that yield porosity characteristics tailored to a specific application. Data-driven approaches, particularly those leveraging machine learning (ML), have emerged as powerful alternatives, enabling efficient exploration of the parameter space and revealing hidden relationships between processing conditions and microstructural outcomes [8, 9]. In LPBF specifically, Gaussian process regression (GPR) has been used to build surrogate models of process–structure–property relationships, including optimized process windows for relative density in LPBF-fabricated AlSi10Mg [10] and predictions of porosity and melt pool depth in stainless steel [11, 12]. In each case, however, the underlying experimental design was fixed a priori (e.g., grid or factorial sampling), so the surrogate could not adapt as data accumulated or concentrate effort where it was most needed. Active learning removes this limitation by using the surrogate's own uncertainty to select each successive experiment, and has been shown to explore complex, expensive-to-sample parameter spaces substantially more efficiently than such static designs in other domains [13–16]. Yet the adaptive paradigm has not been used to guide LPBF experimentation toward characterizing the *full distribution* of defect properties, rather than a single scalar target.

This scalar treatment discards the variability, skewness, and multimodality that distinguish, for instance, a narrow population of small gas pores from a broad, bimodal population containing both gas and lack-of-fusion defects. As one example, mechanical properties, most notably fatigue life, are not dictated by average porosity but rather by extreme-value statistics and the probability distribution tails of large, irregular defects [17–19]. Advanced X-ray computed-tomography investigations have shown that pore-size and pore-morphology distributions, including sphericity and aspect ratio, capture localized stress concentrations and fatigue-crack initiation mechanisms that scalar porosity measures alone can not [20, 21]. Capturing the full statistical distribution of porosity as a continuous function of process parameters is therefore vital for predicting structural reliability in LPBF-fabricated metals. Generative approaches have recently been used to synthesize realistic pore microstructures whose statistical and dimensional properties match experimentally observed porosity distributions [22], but such methods are not conditioned on process parameters and therefore cannot predict how the pore-property distribution changes under untested combinations of laser power and scan velocity. A distributional treatment of pore properties as a continuous function of process parameters, enabling prediction and adaptive experimental design at unobserved conditions, remains unexplored.

The objective of this work is to address both gaps simultaneously by proposing an efficient and scalable framework for parameter-space exploration and defect-characteristic prediction in LPBF processes. Our method leverages a probabilistic machine learning model to estimate the *full statistical distributions* of porosity characteristics, specifically pore sphericity and maximum Feret diameter, as a function of key processing parameters. This is coupled with a distribution-level active learning strategy that adaptively selects new experiments where the surrogate is most uncertain about these distributions. Furthermore, we introduce a principled stopping criterion for adaptive experimental design based on information gain, quantified by the Kullback-Leibler (KL) divergence between the surrogate's predicted porosity distributions, averaged over the parameter space, at successive experimental steps. This approach aims to identify processing conditions that yield predictable, application-specific porosity characteristics, enabling more reliable, targeted, and experimentally efficient process optimization and application-specific process design in LPBF.

Results

Framework overview

The proposed framework integrates experimental characterization, probabilistic modeling, and adaptive experimental design into a unified pipeline for predicting the distribution of pore properties across the LPBF parameter space, as illustrated in Figure 1. In an active learning campaign, the pipeline begins with the fabrication of specimens at a small, randomly selected set of laser power and scan velocity combinations, followed by μ-CT imaging and segmentation to extract individual pore-level measurements of sphericity and maximum Feret diameter. More details are discussed in the Methods section. Although the present study focuses on these two properties as representative descriptors of pore morphology and size, the framework is general and can be readily extended to any quantifiable pore characteristic, such as volume, surface area, or spatial distribution. Rather than summarizing these measurements as a single average value, we model the pore properties for each process-parameter combination as a mixture of lognormal distributions, capturing both the inherent variability and the multimodal characteristics of pore populations arising from distinct defect-formation mechanisms.

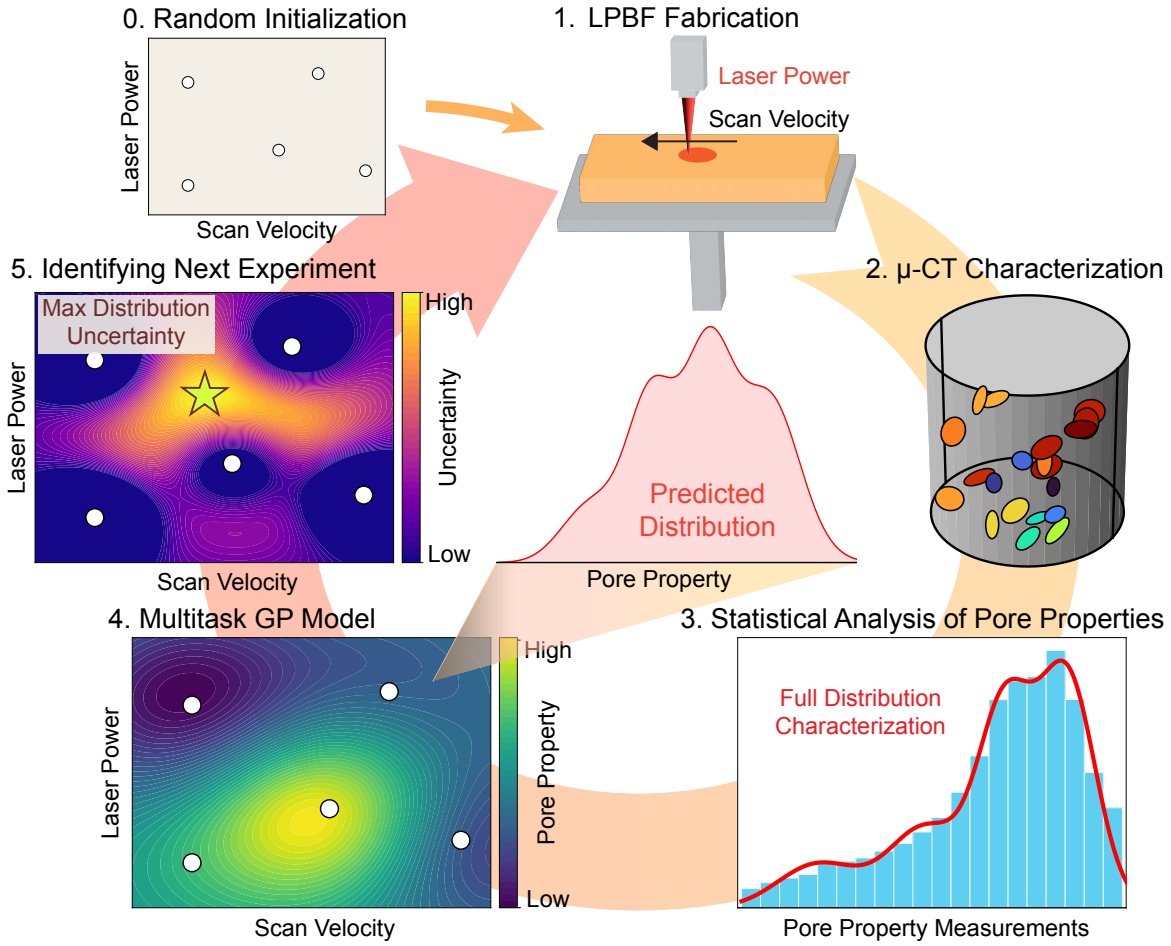

Fig. 1 Overview of the closed-loop active learning framework for pore distribution prediction in LPBF metals. The pipeline consists of six stages: (0) random initialization of a small set of laser power P and scan velocity V combinations; (1) LPBF fabrication of specimens at the selected P-V combinations; (2) μ-CT characterization to extract pore-level measurements; (3) statistical analysis representing pore properties as a full distribution characterization; (4) multitask GPR models that predict the full pore property distribution at any untested point in the parameter space; and (5) identifying the next experiment by selecting the P-V combination with maximum distribution uncertainty. The newly identified experiment is then added to the design set, closing the loop back to stage (1).

The parameters governing these distributions (the component weights, log-means, and log-standard deviations) then serve as training targets for a set of independent multitask Gaussian process models, grouped by pore property and parameter type. Each model takes as input a point in the two-dimensional (2D) processing parameter space $\boldsymbol{x} = \{P, V\}$, defined by laser power P and scan velocity V, and returns as output the corresponding mixture component parameters for that group. Within each GPR model, the mixture components are treated as correlated outputs, allowing the model to transfer information across components and predict complete distributions of pore properties at any untested point in the parameter space. An active learning (AL) loop then guides the sequential selection of new experiments by targeting the greatest epistemic uncertainty in the predicted distribution. We demonstrate that this strategy yields a more accurate distributional characterization of pore properties than grid or random sampling, given the same experimental budget. Finally, we introduce a stopping criterion based on the marginal KL divergence between successive GPR posteriors, which provides a principled, budget-free signal for when the model has converged, and further experimentation is unlikely to yield meaningful new information. In this work, we use a set of 22 of the 24 specimens fabricated in [23] spanning a range of laser power and scan velocity combinations as a case study to demonstrate the stochastic representation of pore properties introduced below and to serve as the ground-truth surrogate for the synthetic active learning campaigns described in later sections (see Methods and [23] for fabrication details and the exclusion criterion). The following subsections describe each component of this framework and present the resulting predictions and benchmarks.

Stochastic representation of pore properties

Fully characterizing the effect of process parameters on AM material quality requires describing pore properties through probability distributions rather than single scalar values. Historically, the literature reports a single representative value for each pore property, such as the mean sphericity or the maximum Feret diameter across all pores in a sample [6]. However, a single LPBF-fabricated specimen can contain hundreds to thousands of pores that vary widely in size and morphology, depending on local processing conditions and the dominant defect-formation mechanism. Reporting only averages conceals this variability and, consequently, important information about material quality. As noted, a full distributional treatment of individual pore-level morphological properties as a continuous function of process parameters remains largely unexplored [22, 24].

A key consideration in choosing an appropriate distribution family is the physical nature of the pore properties being modeled. Pore sizes, quantified here through the maximum Feret diameter, are strictly positive and typically exhibit right-skewed distributions, with a large population of small pores and a long tail of occasional large defects. Similarly, pore sphericity, while bounded on the interval $[0, 1]$, exhibits asymmetric distributions whose shape depends on the dominant defect formation mechanism, ranging from sharp, high-sphericity distributions in the keyhole regime to broad, left-skewed profiles in the lack-of-fusion regime where irregular defects prevail. These characteristics are inconsistent with the symmetric, unbounded support of the normal distribution, which can assign non-negligible probability to physically impossible negative values and fails to capture the asymmetry present in the data. The lognormal distribution, by contrast, is defined on the positive real line, naturally accommodates right-skewed data, and arises theoretically from multiplicative growth processes, consistent with the multiplicative nature of pore growth dynamics during melting and solidification. Note that while sphericity is formally bounded on $[0, 1]$, the lognormal mixture is applied as a practical approximation, justified empirically by the high goodness-of-fit achieved across all 22 samples (Figures S1, S2; Table S1) with negligible probability mass assigned near the boundaries.

Furthermore, pore populations in LPBF materials are rarely homogeneous. Distinct defect formation mechanisms (gas porosity, keyhole porosity, and lack-of-fusion porosity) can coexist within a single sample, each producing pores with characteristic morphologies and size ranges. A single lognormal distribution cannot capture this multimodality. We therefore model pore properties using a mixture of K lognormal distributions, which can simultaneously represent both within-mechanism variability and between-mechanism heterogeneity in pore populations. Formally, for given point

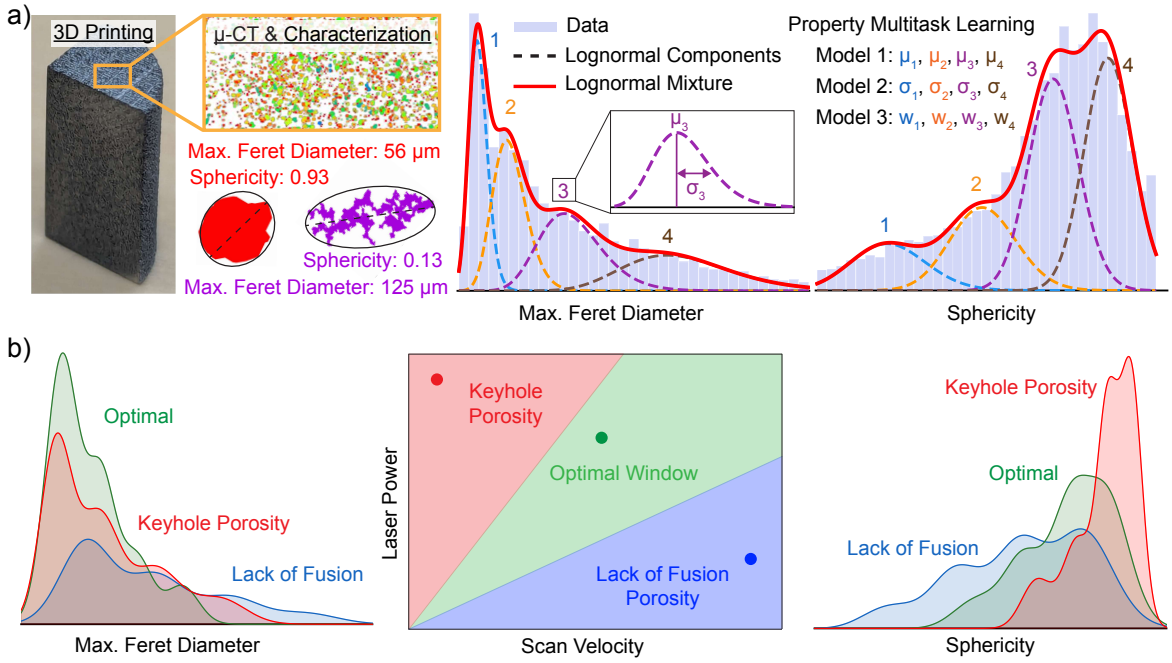

Fig. 2 Stochastic characterization of pore properties in LPBF-fabricated SS316L. (a) Representative μ-CT cross-section of a specimen showing pore morphologies ranging from a near-spherical small gas pore to a highly irregular large lack-of-fusion defect. Histograms of maximum Feret diameter and sphericity of a representative specimen are shown with the fitted four-component lognormal mixture (red solid curve) and its individual components (colored dashed curves, numbered 1–4), as defined in Eq. 1. The inset isolates component 3 to illustrate the log-mean μ_3 and log-standard deviation σ_3 geometrically. The twelve mixture parameters are grouped into three multitask GPR models: Model 1 predicts the four component log-means $\{\mu_k\}$, Model 2 the four log-standard deviations $\{\sigma_k\}$, and Model 3 predicts the four mixture weights $\{w_k\}$, which are constrained to sum to one, for each pore property. (b) Fitted lognormal mixture distributions for maximum Feret diameter (left) and sphericity (right) at three representative process conditions, corresponding to the keyhole porosity (red), optimal window (green), and lack-of-fusion porosity (blue) regimes, with their respective laser power-scan velocity coordinates marked on the process map (center).

$\boldsymbol{x} = \{P, V\}$ in parameter space, the distribution of pore property $\mathcal{P}$ is defined as:

$$\begin{aligned} \mathcal{P}(d \mid \boldsymbol{\phi}(\boldsymbol{x})) &= \sum_{k=1}^{K} w_k(\boldsymbol{x}) \cdot \log \mathcal{N}\left(d \mid \mu_k(\boldsymbol{x}), \sigma_k^2(\boldsymbol{x})\right), \\ &\sum_{k=1}^{K} w_k(\boldsymbol{x}) = 1, \quad w_k(\boldsymbol{x}) \geq 0, \\ &\boldsymbol{\phi}(\boldsymbol{x}) = \{w_k(\boldsymbol{x}), \mu_k(\boldsymbol{x}), \sigma_k^2(\boldsymbol{x})\}_{k=1}^{K}, \end{aligned} \tag{1}$$

where d denotes the pore property value (sphericity or maximum Feret diameter), K is the number of mixture components, $w_k(\boldsymbol{x})$ is the weight of the k-th component, $\mu_k(\boldsymbol{x})$ and $\sigma_k^2(\boldsymbol{x})$ are the log-mean and log-variance of the k-th lognormal component, respectively, and $\boldsymbol{\phi}(\boldsymbol{x})$ collects all mixture parameters governing $\mathcal{P}(\boldsymbol{x})$ at $\boldsymbol{x}$.

The number of mixture components is set to $K = 4$, since it is the most parsimonious model that simultaneously maximizes distributional fit quality across both pore properties, as detailed in Supplementary Table S1. Note that sphericity and maximum Feret diameter are modeled entirely independently throughout this framework, each with its own fitted mixture and its own set of GPR surrogates; in principle, each property could therefore be assigned a different number of mixture components K, and the shared value of $K = 4$ adopted here reflects a convenient, empirically supported coincidence between the two properties (Supplementary Table S1) rather than a modeling constraint. With $K = 4$ components, $\boldsymbol{\phi}(\boldsymbol{x})$ as defined in Eq. 1 lists four log-means, four log-variances, and four

weight components, for a total of 12 parameters governing $\mathcal{P}(d \mid \boldsymbol{\phi}(\boldsymbol{x}))$. However, the simplex constraint $\sum_{k=1}^{K} w_k = 1$ means the four weights are not all independent; only three can vary freely, with the fourth determined by the constraint. The full distribution is therefore characterized by 11 free parameters—four log-means, four log-variances, and three independent weights—all of which are treated as unknown continuous functions of the process parameters $\boldsymbol{x}$ and predicted using Gaussian process models (Methods). These three independent weights are reparameterized as unconstrained variables $\{z_i(\boldsymbol{x})\}_{i=1}^{3}$ prior to GPR modeling, as detailed in Eq. 5 in the Methods section.

The distributional modeling choices described above are empirically supported by measured pore data across the experimental parameter space. Figure 2 illustrates the stochastic characterization pipeline of pore properties. Figure 2a shows a representative μ-CT cross-section of a fabricated SS316L specimen, with individual pore morphologies spanning the full range from near-spherical gas pores (sphericity 0.93, maximum Feret diameter 56 µm) to highly irregular lack-of-fusion defects (sphericity 0.13, maximum Feret diameter 125 µm). Alongside, histograms for a representative keyhole-regime sample (350 W, 400 mm/s) are shown together with the fitted four-component lognormal mixture. Figure 2b shows the fitted mixture distributions for three distinct process parameter regimes—keyhole porosity (350 W, 400 mm/s), optimal window (300 W, 700 mm/s), and lack-of-fusion porosity (195 W, 1110 mm/s)—demonstrating that the full distributional shape shifts substantially across the parameter space in ways that scalar summary statistics cannot capture.

The histograms confirm the skewed, multimodal character of the pore property distributions and demonstrate that the mixture of lognormals captures the data substantially better than a single lognormal distribution, particularly in the lack-of-fusion and keyhole regimes where two or more defect populations coexist within a single sample, as evidenced by the multimodal character of the fitted mixture components. Figures S1 and S2 show the complete set of fitted lognormal mixtures for all 22 experimental samples.

Notably, the sphericity distribution shifts from a broad, left-skewed profile in the lack-of-fusion regime—reflecting the prevalence of irregular, elongated defects—to a sharp, high-sphericity peak in the keyhole regime where gas pores dominate. The maximum Feret diameter distributions similarly contract and shift toward smaller values as processing conditions improve.

GPR fits of sphericity and maximum Feret diameter

Gaussian process regression is used to predict the full distributions of pore properties continuously across the parameter space, enabling characterization at untested process conditions. The six multitask GPR models described below are trained on the lognormal-mixture parameters fitted to the experimentally measured pore populations at the 22 fabricated specimens introduced above, over a parameter space spanning laser power (180–360 W) and scan velocity (300–1200 mm/s). For each pore property, three multitask GPR models predict the mixture distribution $\mathcal{P}(d \mid \boldsymbol{\phi}(\boldsymbol{x}))$ defined in Eq. (1): one for the four log-means $\{\mu_k(\boldsymbol{x})\}_{k=1}^{4}$, one for the four log-variances $\{\log \sigma_k^2(\boldsymbol{x})\}_{k=1}^{4}$, and one for the three unconstrained weight parameters $\{z_i(\boldsymbol{x})\}_{i=1}^{3}$, with the mixture components serving as correlated tasks within each model. Across both pore properties, this yields six GPR models in total, each predicting a subset of the 11 free parameters of $\boldsymbol{\phi}(\boldsymbol{x})$ at any point $\boldsymbol{x} = \{P, V\}$ per pore property.

Figure 3 shows the GPR-predicted mixture mean and standard deviation of pore sphericity and maximum Feret diameter continuously across the laser power and scan velocity parameter space, with white markers indicating the 22 experimental samples used for GPR training. The predictions reveal three distinct regions that are consistent with the known defect-formation mechanisms in LPBF. In the low-power, high-velocity region, the mixture mean sphericity is minimized, and the mixture mean diameter is maximized, with both exhibiting elevated standard deviations. These predictions are consistent with severe lack-of-fusion defects, where insufficient energy density prevents complete powder melting, resulting in large, irregular pores with highly variable morphologies [20]. The elevated standard deviation in this region reflects the instability of the melting process and the coexistence of multiple defect populations within a single sample.

In the high-power, low-velocity region, GPR predicts high sphericity and moderate-to-large pore sizes with low variability. This is consistent with keyhole porosity, where excessive energy density creates an overheated, highly fluid melt pool in which collapsing vapor depressions are rapidly rounded

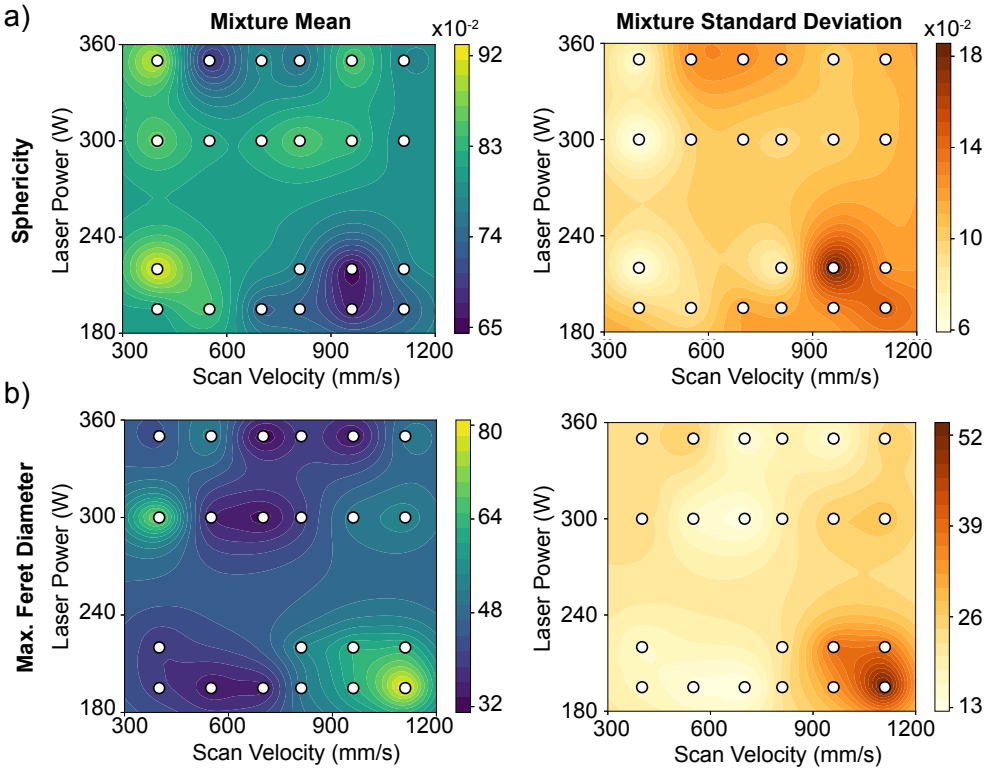

Fig. 3 GPR-predicted mixture distribution statistics across the laser power and scan velocity parameter space for (a) sphericity and (b) maximum Feret diameter. Both quantities are computed from the predicted four-component lognormal mixture at each point in the parameter space. White markers indicate the 22 experimental samples used for GPR training. Both properties vary systematically with laser power and scan velocity, consistent with the known keyhole, optimal, and lack-of-fusion regimes for defect formation discussed in the text.

by surface tension before the solidification front arrives [20]. The consistently high sphericity and low standard deviation in this region confirm that keyhole pores, while large, are morphologically uniform, a physically expected consequence of the extreme melt pool fluidity at high energy densities.

The optimal processing window is in the intermediate-power and low-to-medium-velocity region, where the predicted pore sizes are smallest, and the mixture standard deviation of both pore properties is minimized, reflecting a stable, reproducible melting process. The moderate-to-high sphericity in this region is consistent with the dominance of small gas pores inherited from the powder feedstock, which spheroidize under surface tension forces in the stable, low-viscosity melt pool. While the mixture mean sphericity in the optimal window is slightly lower than in the keyhole regime, this is physically expected. In the keyhole regime, the extreme fluidity of the overheated melt allows surface tension to rapidly round collapsing vapor cavities into highly spherical voids [20, 25], whereas in the optimal regime, sphericity is governed by the slower equilibration of smaller gas pores in a cooler, more viscous melt pool. The critical distinction between the two regimes is therefore not sphericity alone but the combination of pore size, sphericity, and process stability [26], all of which are simultaneously optimized in the optimal processing window.

To assess the predictive accuracy of the multitask GPR models, leave-one-out cross-validation (LOO-CV) was performed on the 22 samples used in this study. For each held-out sample, the six GPR models are retrained on the remaining 21 samples and then used to predict the full lognormal mixture distribution at that location. The LOO-CV results are summarized in Figure 4, where the yellow histogram shows the measured pore data, the orange dashed curve is the lognormal mixture fitted directly to the experimental data, and the purple solid curve is the GPR-predicted mixture distribution. Background colors indicate the three defect formation regimes identified in Figure 3: keyhole porosity (red), optimal processing window (green), and lack-of-fusion porosity (blue).

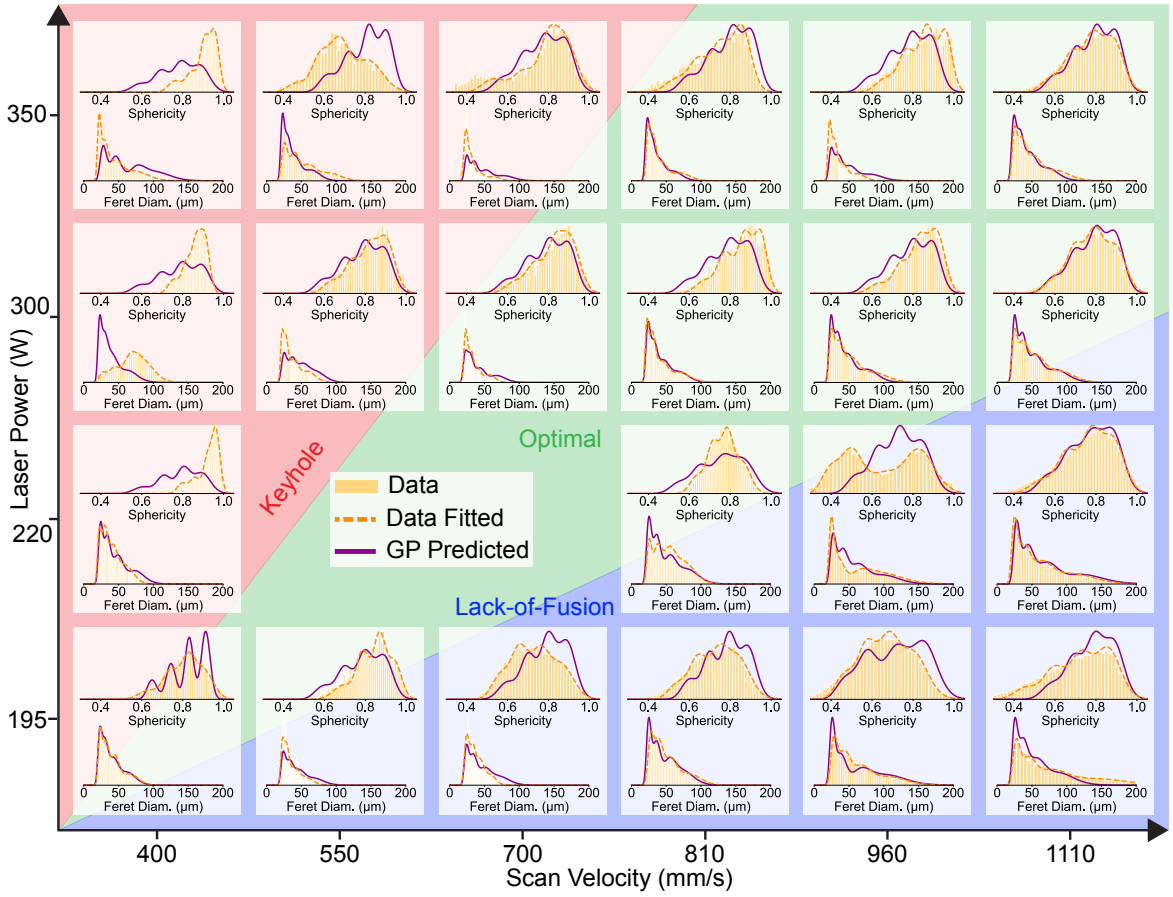

Fig. 4 Leave-one-out cross-validation results for the GPR-predicted lognormal mixture distributions of pore sphericity and maximum Feret diameter at each experimental sample location, arranged in the laser power–scan velocity parameter space. At each location, the six GPR models are retrained on the remaining 21 samples and used to predict the full mixture distribution at the held-out point. The yellow histogram shows the measured pore data, the orange dashed curve is the lognormal mixture fitted directly to the experimental data, and the purple solid curve is the GPR-predicted mixture distribution. Background colors indicate the three defect formation regimes: keyhole porosity (red), optimal processing window (green), and lack-of-fusion porosity (blue). The results show that the GPR-predicted mixture distributions are generally in close agreement with the data-fitted lognormal mixture, except for some points where the data show significant changes from their neighboring points.

Figure 4 shows that the GPR-predicted mixture distributions are in close agreement with the data-fitted distributions across the majority of the parameter space. This demonstrates the surrogate model's ability to accurately interpolate the full pore-size and morphology distributions at unobserved processing conditions. Importantly, the GPR models correctly capture regime-dependent changes in the distribution's shape across the parameter space. In the keyhole and optimal regimes, the predicted sphericity and diameter distributions exhibit sharp, relatively narrow peaks concentrated at high sphericity values and small pore sizes, consistent with a homogeneous population of small, near-spherical pores. Similarly, the GPR correctly predicts broader, right-skewed distributions in the lack-of-fusion regime, reflecting the presence of large, irregular pores with high morphological variability. The GPR's ability to reproduce these regime-dependent distributional shifts indicates that the multitask structure successfully captures how the mixture parameters co-vary across the parameter space, rather than treating each parameter as an independently interpolated quantity.

The agreement is particularly strong in the interior of the parameter space, where the spatial variation in pore distributions is smooth and the GPR benefits from dense neighboring training points. Larger discrepancies are observed near the regime boundaries, where pore morphology transitions more rapidly and the GPR has fewer neighboring training points to draw from. A related effect occurs

at the corners of the sampled parameter space (e.g., the highest-power/lowest-velocity and lowest-power/lowest-velocity combinations), where predictive accuracy is limited less by regime transitions than by the reduced number of neighboring training points on all sides, a structural consequence of the boundary of the sampled design rather than of the underlying physics. A notable case occurs at 300 W and 400 mm/s, where the measured diameter distribution is shifted toward larger pore sizes relative to its neighbors at the same scan velocity—a trend not reproduced by the GPR prediction, which instead follows the spatial trend established by the surrounding training points. This suggests that this sample may represent a local outlier rather than a genuine spatial trend in the parameter space.

Parameter space exploration using active learning

Having established that the multitask GPR models accurately recover the full pore property distributions across the parameter space, we now turn to how to efficiently select experiments to achieve this accuracy. Active learning, where experiments are chosen successively to maximize information gain, has been shown to explore complex parameter spaces more efficiently than non-adaptive strategies such as grid and random sampling [13–16]. This efficiency is particularly valuable in LPBF, where each experiment requires fabrication, μ-CT scanning, and segmentation, making exhaustive sampling of the synthesis parameter spaces impractical. While grid sampling guarantees uniform coverage, it does not exploit information accumulated during the campaign and therefore allocates experimental effort independently of where the model is most uncertain. Here, we demonstrate that an active learning approach, by jointly targeting the regions of highest predicted uncertainty in both sphericity and maximum Feret diameter, yields a more accurate characterization of pore property distributions than either grid or random sampling, given the same experimental budget.

To ensure statistically sound, comparable results across the three sampling approaches, active learning, grid, and random, synthetic experimental campaigns are conducted under identical conditions. Synthetic experiments are performed by sampling from the GPR models shown in Figure 3. Because these models are fitted to the experimentally measured pore populations, they encode physically realistic trends across the parameter space and can therefore be treated as ground-truth models. This allows multiple parameter-space exploration campaigns to be run with different initial points and exploration trajectories, capturing variability without incurring the time and cost of additional physical experiments. For each approach, 30 campaigns are run, each representing a complete effort for exploring the parameter space. Each campaign starts by randomly selecting and synthetically testing 5 points in the parameter space. The synthetic experimental results are collected for these points, where the distributions of sphericity and maximum Feret diameter are characterized for each point, and 6 multitask GPR models are fitted to the synthetic data. After that, a new point is identified, a synthetic experiment is performed, and the 6 GPR models are refitted. This loop repeats for 30 steps.

Identifying new experiments for each campaign depends on the approach taken. The active learning approach selects the point in the parameter space that maximizes a distribution-level epistemic uncertainty criterion, summed over the two morphological properties. For each property, the uncertainty is not the raw variance of any single GPR; instead, the three GPRs governing that property's mixture parameters are sampled jointly from their epistemic posteriors, and each joint sample is mapped to a full lognormal-mixture probability density over the property's support. The uncertainty for that property is then the probability-mass-weighted integral of the pointwise variance of these densities across the posterior ensemble (Eq. 7), capturing disagreement about the *shape* of the predicted distribution weighted by where probability mass actually lies. The two per-property uncertainties are each normalized by a precomputed scale and then summed (Eq. 8); the point that maximizes this combined score is chosen as the next experiment. Both properties are included because each new experiment simultaneously characterizes both distributions. Figure 5a illustrates this acquisition function schematically, and for full procedural details (e.g., posterior sampling and optimization), readers are referred to the Methods section. In the grid sampling approach, new experiments are randomly sampled without replacement from a 6×6 grid. In the random sampling approach, points are selected at random from the parameter space.

To evaluate the accuracy of each campaign, the GPR-predicted pore property distributions are compared against the ground-truth distributions at a fixed set of 100 test points, generated using a Latin hypercube design to ensure uniform, space-filling coverage of the parameter space (Figure S3). This test set is held out from all campaigns and is identical across the three approaches and all 30 trials, so that differences in performance reflect the exploration strategy rather than the choice of evaluation points. Because the quantity of interest at each test point is a full probability distribution rather than a single scalar, conventional pointwise error metrics such as the root-mean-square error (RMSE) are inadequate. RMSE compares only point estimates (e.g., the mean), discarding the shape, spread, skewness, and multimodality that distinguish, for instance, a narrow keyhole-regime distribution from a broad, multimodal lack-of-fusion distribution. We therefore quantify accuracy using three distribution-level metrics that compare the predicted lognormal mixture with the ground-truth mixture. The *Wasserstein-1 distance* measures the minimal "work" required to transform the predicted distribution into the ground truth and is sensitive to discrepancies in both location and shape, with lower values indicating closer agreement. The *Kullback–Leibler (KL) divergence* quantifies the information loss when the predicted distribution approximates the ground truth, strongly penalizing predictions that assign low probability to regions where the true distribution is high; lower values indicate a better fit. The *log predictive density (LPD)* measures the average log-likelihood that the predicted distribution assigns to samples drawn from the ground truth, directly rewarding accurate predictive distributions; higher values indicate better performance. Together, these three metrics assess distributional agreement from complementary perspectives, including geometry, information theory, and predictions, providing a more complete and rigorous evaluation than any single scalar error could.

Figure 5 recaps the acquisition function schematically (panel a, as described above) and reports the resulting distributional accuracy metrics for the three sampling strategies for sphericity (panels b–d). Figure 5b–d report the mean of each accuracy metric as a function of experimental step, averaged over the 30 campaigns, with shaded bands denoting ± one standard error of the mean evaluated against the ground-truth distributions described above. Across all three metrics, the active learning approach consistently outperforms both grid and random sampling, achieving a given level of accuracy in fewer experiments, with the largest advantage at small-to-moderate budgets. The improvement is most pronounced for the KL divergence (Figure 5c), where active learning clearly separates from both baselines within the first ten experiments and maintains its advantage throughout the campaign. A similar advantage is evident in the Wasserstein distance and log predictive density (Figure 5b, d), though the separation between strategies emerges somewhat more gradually than for KL divergence. Grid sampling consistently ranks second, outperforming random sampling because its uniform coverage avoids the redundant, clustered queries that random selection occasionally produces; however, it remains inferior to active learning because it cannot adapt to where the model is most uncertain, allocating experiments evenly even in regions where the pore property distributions are already well characterized. By contrast, active learning allocates its experimental budget to the regions of highest uncertainty, where additional measurements are most informative.

The corresponding results for maximum Feret diameter, shown in Figure S4, displays the same qualitative trends observed for sphericity (Figure 5b-d). The separation between the three strategies is nonetheless narrower than is typical in higher-dimensional exploration problems, and by the later stages of the campaign, the gap between active learning and grid sampling becomes small relative to the gap between either method and random sampling. We attribute this to two related factors. First, all three strategies use an identical multitask GPR architecture to fit the collected data; the only difference between them is which points are selected for training, not how the surrogate interprets those points once observed. Once a reasonable number of points has been distributed across the space, the resulting surrogates are therefore of comparable quality, and the advantage of active learning is confined to where points are placed rather than to any difference in modeling capacity. Second, the P–V parameter space explored here is only two-dimensional and relatively modest in extent, so it can be filled efficiently by any structured strategy. In low dimensions, a grid (here, 6×6 points) already provides close to uniform coverage with comparatively few samples, and an uncertainty-based acquisition function operating on a smooth GPR posterior tends to spread its queries across the domain in

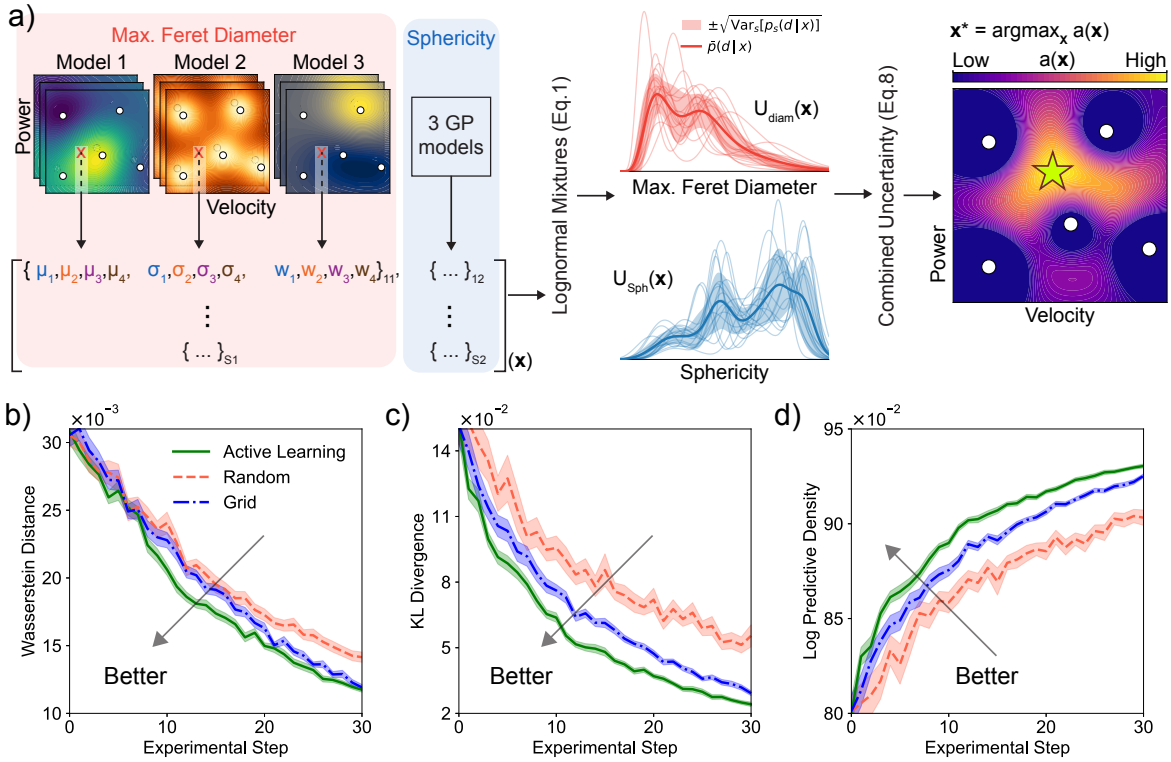

Fig. 5 Distribution-level acquisition function and active learning performance for sphericity. (a) Schematic illustrating the epistemic-uncertainty acquisition function. For each pore property, three multitask GPR models take the process parameters $\boldsymbol{x} = \{P, V\}$ as input and predict the 12 parameters that govern that property's lognormal mixture distribution (Eq. 1). At a candidate point $\boldsymbol{x}$, these models are sampled jointly from their epistemic posteriors, and each joint sample is mapped to a full lognormal-mixture density over the property's support, yielding an uncertainty score $U_{\mathrm{diam}}(\boldsymbol{x})$ and $U_{\mathrm{Sph}}(\boldsymbol{x})$ (Eq. 7), shown here for maximum Feret diameter (red) and sphericity (blue) as an ensemble of posterior realizations (thin curves) together with the posterior-mean density (thick solid line) and pointwise ensemble standard deviation (shaded band). The two per-property scores are normalized and summed into the combined acquisition score $a(\boldsymbol{x})$ (Eq. 8), shown at right across the laser power–scan velocity parameter space. White markers denote previously sampled points, and the star marks $\boldsymbol{x}^* = \arg\max_{\boldsymbol{X}} a(\boldsymbol{x})$, the next selected experiment. (b–d) Active learning (green, solid) outperforms random (red, dashed) and grid (blue, dash-dot) sampling in characterizing the pore sphericity distribution, via (b) Wasserstein-1 distance, (c) KL divergence, and (d) log predictive density as a function of experimental step. Curves show the mean across 30 independent trials; shaded bands denote ± one standard error of the mean, and gray arrows indicate the direction of improving accuracy. Corresponding results for maximum Feret diameter are provided in Supplementary Figure S4.

a qualitatively similar way, since regions far from existing observations are, almost by construction, also the regions of highest predictive uncertainty. Grid sampling and active learning, therefore, fill the two-dimensional parameter space in a broadly similar manner, particularly once the initial random points have seeded the design space, and the two strategies converge toward comparable coverage patterns despite differing selection logic. Random sampling remains more susceptible to clustering and coverage gaps, even at this low dimensionality, which is why it consistently underperforms both structured approaches. We expect the advantage of active learning over grid sampling to grow substantially in higher-dimensional process spaces (e.g., incorporating hatch spacing, layer thickness, or preheat), where a grid fine enough to match the coverage achieved here would require a combinatorially larger number of points, whereas an uncertainty-guided acquisition function scales its exploration to where it is genuinely needed rather than paying the curse of dimensionality.

Having established that the distribution-level active learning acquisition function accelerates parameter space exploration (Figure 5), we evaluate the intrinsic stopping diagnostic defined in Eq. 10 to determine when an experimental campaign reaches convergence without relying on an external ground truth. Figure 6 presents the cumulative information gain ($I_{\mathrm{cumulative},t}$) across experimental

steps, averaged over 30 independent trials for both maximum Feret diameter and sphericity. Because this diagnostic is intended to signal convergence of an adaptive, uncertainty-driven campaign, it is evaluated only for the active learning strategy. Grid and random sampling select points independently of the model's current uncertainty, so a diminishing marginal KL divergence along their trajectories would not indicate genuine convergence of the surrogate, but merely the incidental placement of the next fixed-design point.

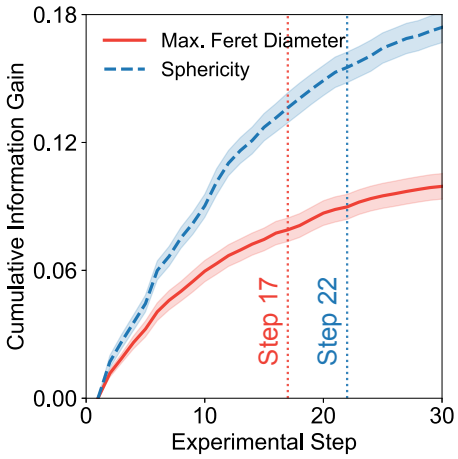

Fig. 6 Automated stopping criterion for active learning campaigns. Cumulative information gained ($I_{\text{cumulative}}$, characterized by cumulative KL divergence) across experimental steps for maximum Feret diameter (red, solid) and sphericity (blue, dashed). Shaded regions denote ± one standard error of the mean across $N = 30$ independent active learning trials. Dotted vertical lines indicate the automated stopping step t^* triggered when the marginal information gain drops below 2.5% of the total cumulative information acquired up to that point ($I_{\text{marginal},t^*} < 0.025 \times I_{\text{cumulative},t^*}$). The stopping criterion was triggered at Step 17 for maximum Feret diameter and Step 22 for sphericity.

During early experimental iterations ($t < 10$), each newly sampled parameter combination yields substantial marginal information gain ($I_{\text{marginal},t}$), as reflected in the steep initial slopes of both cumulative curves. As the active learning loop targets areas of highest epistemic uncertainty and the multitask GPR surrogate consolidates its predictive posterior across the parameter space, the information gain systematically diminishes. Applying our 2.5% relative information gain threshold ($I_{\text{marginal},t^*} < 0.025 \times I_{\text{cumulative},t^*}$), maximum Feret diameter triggered the stopping criterion at Step 17, indicating that the predictive posterior had largely stabilized, with subsequent steps contributing diminishing updates. Sphericity required slightly broader exploration due to the complex, multimodal transition from irregular lack-of-fusion pores to rounded gas defects, which triggered the stopping condition at step 22. Since each experiment simultaneously informs both property distributions, a practical campaign would continue testing until both criteria are satisfied, here, Step 22, governed by the slower-converging property (sphericity). These results confirm that tracking relative information gain provides an intuitive, data-driven stopping signal that prevents redundant physical experiments while ground-truth accuracy metrics (Figure 5) continue to improve modestly beyond these steps, so the criterion identifies the point of diminishing returns rather than exact convergence, and the threshold (2.5%) can be tightened or relaxed depending on experimental cost.

Conclusion

Characterizing porosity remains a major concern in the metal AM community. Porosity is a defect to be minimized in load-bearing parts, but a designed feature in applications such as biomedical implants and energy generation and storage devices. In either case, the key to controlling porosity is accurately quantifying its characteristics, which enables the development of tailored materials for the application of interest. Although porosity is an active field of research, a gap remains in capturing the full

distributions of these characteristics. In this study, we presented a stochastic representation of porosity characteristics that enables their more accurate quantification. We modeled the pore sphericity and maximum Feret diameter in SS316L additively manufactured samples as each following a lognormal mixture distribution, and we quantified these full distributions at any point in the laser power–scan velocity parameter space. We showed that active learning based on multitask Gaussian process models and an acquisition function based on distributional uncertainty enables efficient exploration and accurate quantification of the pore properties distributions across the parameter space. The major contributions of this study include:

- Stochastically quantifying and predicting the distributions of porosity characteristics across the parameter space;
- Implementing multitask GPR modeling for potentially correlated outputs;
- Demonstrating a distributional, information-based acquisition function for active learning;
- Developing a distribution-level information-theoretic stopping criterion for experiments;
- Providing an approach readily extensible to any porosity characteristic and distribution family.

Several limitations of this work suggest directions for future research. First, our active-learning strategy was validated against a ground-truth surrogate constructed from the available experimental data rather than in a closed loop with new physical builds. Demonstrating the approach with real experiments is a natural next step toward in-process deployment. Second, we restricted the parameter space to laser power and scan velocity, holding other process parameters (e.g., hatch spacing, layer thickness, and preheat) fixed. Extending the framework to a higher-dimensional parameter space would broaden its applicability and, as discussed in the Results, is where the advantage of active learning over grid sampling is expected to be most pronounced, since a grid fine enough to match adaptive coverage becomes combinatorially expensive as dimensionality increases, whereas the uncertainty-guided acquisition function scales its exploration only to where it is needed. Third, we assumed a lognormal mixture as the parametric family for both pore characteristics. While this family fit our data well, other characteristics or material systems may be better described by different families, and incorporating model selection over distribution families would make the approach more general. Fourth, while we focused on sphericity and maximum Feret diameter, pore connectivity, spatial clustering, and orientation are also consequential for functional performance and could be incorporated as additional tasks within the same multitask framework. Finally, the model describes the distribution of pore properties given that pores are present, and does not model pore number or volume fraction. Near-fully-dense conditions, where the pore population is too sparse to define a distribution, lie outside its domain, and predictions near the two excluded conditions rely on interpolation from neighboring specimens.

Methods

Experimental data generation

Gas-atomized ExOne powder with a particle size distribution of 20–53 µm was used to fabricate the SS316L samples. The builds were carried out on a TruPrint 3000 system. To isolate the influence of laser power and scan velocity, the hatch spacing, layer thickness, and laser spot diameter were kept constant at 150 µm, 30 µm, and 100 µm, respectively. Only laser power and scan velocity were varied, allowing the production of samples with distinct pore characteristics. In LPBF, alterations in laser power and velocity directly affect the pore structure of the printed components, as shown in Figure 2(b). To obtain the necessary pore variation for the GPR models, the sample process parameters were adjusted to capture different pore variations on the printed parts. The process parameters of the samples are shown as the white markers in Figure 3. A preheat temperature of 200 °C and a 67-degree scan rotation were also used, with no contour scans, upskin, or downskin during printing.

The dataset of ref. [23] comprises 24 specimens. Two further specimens (220 W at 550 and 700 mm/s) were excluded from surrogate training. These near-fully dense specimens contain only small pores, and the 700 mm/s specimen's maximum Feret diameters span just 17.5-37.5 µm (3.5-7.5 voxels),

so its size distribution is dominated by voxel discretization and is not meaningfully resolved by a four-component mixture. They also fall outside the porosity-engineering regime that is the focus of this work. Fit statistics in Table S1 are reported for all 24 specimens.

Micro-CT and data analysis

Micro–computed tomography (μ-CT) was employed to examine the internal defect structure of the samples non-destructively using a Nikon XTH 225 ST system at the Utah State University μ-CT facility. The specimens were mounted in a sample holder and scanned with a beam energy of 135–145 kV and a beam current of 55–65 µA. An exposure time of 1.42 s was used during acquisition, and the samples were positioned at a slight angle to reduce edge artifacts. The scans were conducted with an effective pixel size of 5 µm to obtain high-resolution images of the internal features. For each specimen, 2300 projections were acquired to reconstruct the three-dimensional volume. The projection data were subsequently reconstructed using CT-Pro software to generate TIFF image stacks, which were then used for further analysis.

The collected μ-CT data were analyzed using Object Research Systems (ORS) Inc.'s Dragonfly 2022.2 software [27]. The software was used to segment the reconstructed volumes into defect and metallic regions using its built-in machine learning-based segmentation tools. Following segmentation, morphological operations were applied to prepare the data for quantitative analysis. To reduce the influence of noise and improve measurement reliability, segmented features smaller than 8 voxels were removed from the dataset. After filtering, a 26-connectivity algorithm was applied to identify and label individual connected components within the volume. This approach allowed each defect to be isolated and quantified separately. Using Dragonfly's built-in analysis tools, several defect descriptors were extracted, including pore maximum Feret diameter and sphericity, and were used as the properties for this study. For more information, interested readers are referred to [23].

Gaussian process regression

Gaussian process regression (GPR), a machine learning model, is used to characterize the distributions of pore properties in AM-printed materials. We choose GPR because it is well-suited for stochastically modeling the unknown latent relationship (function) between process parameters and observable properties, like pore sphericity, even when only limited data are available relative to the size of the parameter space. The GPR also quantifies the uncertainty of its predictions, offering valuable insights into their reliability. Its stochastic nature allows for the differentiation between the aleatoric uncertainty (related to the inherent data variability) and epistemic uncertainty (related to the availability of training data for accurate predictions). As discussed below, the GPR model is defined entirely by three building blocks: the prior mean, the noise, and the kernel functions. Each of these functions depends on hyperparameters, assembled in the set $\boldsymbol{\theta}$, that offer clear insights into the nature of the underlying relationship being modeled, thereby enhancing the interpretability of the GPR model. Another favorable characteristic is the ability to tailor the smoothness of the modeled function by selecting and tuning the kernel function. Overall, much work has shown the approximation power of GPR models of unknown relationships [28–30].

The parameter space $\boldsymbol{X} \subset \mathbb{R}^2$ here is a subdomain of the two-dimensional (2D) Euclidean space spanning laser power (x_1) and scan velocity (x_2). These two parameters are chosen because they have been shown to control the porosity properties of AM-printed materials [3, 7]. This parameter space is bounded by the limits of the TruPrint 3000 AM LPBF printer. Specifically, we consider laser power between 180 W and 360 W and scan velocity between 300 mm/s and 1200 mm/s.

Single-output GPR

We first describe the GPR model for a single scalar output, then generalize it to the multitask setting used in this work. A single latent function $f(\boldsymbol{x})$ can only be sampled via noisy measurements $y(\boldsymbol{x}) = f(\boldsymbol{x}) + \epsilon(\boldsymbol{x})$, with $\epsilon(\boldsymbol{x})$ being an identically and independently distributed noise modeled as $\mathcal{N}(0, \sigma_n^2(\boldsymbol{x}))$ and $\sigma_n^2(\boldsymbol{x})$ the noise variance. Mathematically, GPR modeling is a Bayesian method that requires a prior distribution over the latent function values, $\boldsymbol{f} = f(\boldsymbol{x}_i)\ \forall\, i \in \{1, 2, \ldots, n\}$, where n is the number

of data points, and a likelihood to calculate the posterior distribution (GPR predictions). The GPR prior is a multivariate normal probability distribution $p(\boldsymbol{f}) \sim \mathcal{N}(\mathrm{E}[\boldsymbol{f}], \mathrm{Cov}[\boldsymbol{f}, \boldsymbol{f}])$ over $\boldsymbol{f}$. Any finite subset of function values follows a normal distribution. This multivariate distribution is characterized by a mean vector $\mathrm{E}[\boldsymbol{f}] = \boldsymbol{\mu} = \mu(\boldsymbol{x}_i; \boldsymbol{\theta})$ and a covariance matrix $\mathrm{Cov}[\boldsymbol{f}, \boldsymbol{f}] = \boldsymbol{K} = k(\boldsymbol{x}_i, \boldsymbol{x}_j; \boldsymbol{\theta})\ \forall\, i, j$, where k is the positive semi-definite kernel function acting on pairs of inputs $\boldsymbol{x}_i, \boldsymbol{x}_j$. In addition to the prior, the GPR requires a likelihood model of the noisy measurements, $p(\boldsymbol{y}|\boldsymbol{f}, \boldsymbol{\theta}) = \mathcal{N}(\boldsymbol{f}, \boldsymbol{V}(\boldsymbol{\theta}))$, where $V_{ii} = \sigma_n^2(\boldsymbol{x}_i; \boldsymbol{\theta})$ defines the diagonal noise matrix. Marginalizing over the unknown function values $\boldsymbol{f}$ and conditioning on the data $\boldsymbol{y}$ yields the posterior $p(\boldsymbol{f}^*|\boldsymbol{y}, \boldsymbol{\theta})$, where $\boldsymbol{f}^*$ are the predictions.

In practice, defining a GPR model requires defining the prior mean, noise, and kernel functions. The prior mean encodes the expected trend of the latent function before data collection; starting from an uninformed prior, it is taken to be a constant, $\mu(\boldsymbol{x}_i; \boldsymbol{\theta}) = c$. The noise function quantifies the variability of $\boldsymbol{y}$, allowing the estimation of aleatoric uncertainty via the noise variance. Here, we consider the noise to be homoscedastic and independent of the location in the parameter space, $\sigma_n^2(\boldsymbol{x}_i; \boldsymbol{\theta}) = \sigma_n^2$. Finally, the kernel function $k(\boldsymbol{x}_i, \boldsymbol{x}_j; \boldsymbol{\theta})$ is the main building block of the GPR model, as it dictates the properties of the latent function predictions (e.g., smoothness), acts as the covariance operator, and estimates the epistemic uncertainty that is crucial when deciding which points $\boldsymbol{x}$ to sample next. Here, we adopt a stationary Matérn kernel with smoothness parameter $\nu = 3/2$. By stationary, we mean that the computed covariance between two function values depends only on the distance between their corresponding points in the parameter space. For more information about stationary and non-stationary kernel functions, interested readers are referred to [31, 32]. With this description, the single-output GPR model is defined as:

$$y(\boldsymbol{x}) = f(\boldsymbol{x}) + \epsilon, \tag{2a}$$

$$f(\boldsymbol{x}) \sim \mathcal{GP}\big(\mu(\boldsymbol{x}) = c,\ k_{\nu=3/2}(\boldsymbol{x}_i, \boldsymbol{x}_j)\big)\,, \tag{2b}$$

$$k_{\nu=3/2}(\boldsymbol{x}_i, \boldsymbol{x}_j; \boldsymbol{\theta}) = \sigma_s^2 \left(1 + \sqrt{3}\, r_{ij}\right) \exp\!\left(-\sqrt{3}\, r_{ij}\right), \tag{2c}$$

$$r_{ij} = \sqrt{\sum_{d=1}^{2} \frac{(x_{i,d} - x_{j,d})^2}{l_d^2}}, \tag{2d}$$

$$\epsilon \sim \mathcal{N}(0, \sigma_n^2), \tag{2e}$$

where σ_s^2 is the signal variance that controls the amplitude of the epistemic uncertainty, r_{ij} is the anisotropic distance between $\boldsymbol{x}_i$ and $\boldsymbol{x}_j$, and l_1 and l_2 are the kernel length scales that control the covariance decay in the laser power and scan velocity dimensions, respectively. The single-output set of hyperparameters is thus $\boldsymbol{\theta} = \{c, \sigma_n^2, \sigma_s^2, l_1, l_2\}$, which is learned by the maximum likelihood estimation (MLE) method.

Multi-task GPR

The pore property distributions in this work are not characterized by a single scalar but by multiple correlated mixture parameters at each $\boldsymbol{x}$, and modeling each parameter with an independent GPR model would lose the information shared between them. Multitask GPR addresses this by jointly modeling several outputs (tasks) under a common covariance structure, enabling information transfer across tasks. The key assumption is that the tasks may be statistically dependent. If they are genuinely correlated, the model learns and exploits that correlation to improve predictions for all tasks, whereas if they are effectively independent, the model can recover that limit and treat them separately. Capturing this requires a kernel that encodes both the similarity between points in the input space and the correlation between tasks, each with its own set of hyperparameters.

To this end, we use a Linear Model of Coregionalization (LMC), in which the covariance between the value of task τ at point $\boldsymbol{x}_i$ and the value of task τ' at point $\boldsymbol{x}_j$ factorizes into an input-space kernel and a task (coregionalization) kernel:

$$k_{\mathrm{LMC}}((\boldsymbol{x}_i, \tau), (\boldsymbol{x}_j, \tau')) = k_{\nu=3/2}(\boldsymbol{x}_i, \boldsymbol{x}_j)\, B_{\tau\tau'}, \tag{3}$$

where $k_{\nu=3/2}$ is the Matérn kernel (Eq. 2c) and $\boldsymbol{B} \in \mathbb{R}^{T\times T}$ is the symmetric positive semi-definite task covariance matrix over the T tasks of the model. The task matrix is parameterized as:

$$\boldsymbol{B} = \boldsymbol{w}\boldsymbol{w}^\top + \mathrm{diag}(\boldsymbol{\kappa}), \tag{4}$$

where $\boldsymbol{w} \in \mathbb{R}^T$ is a vector of coregionalization weights whose outer product $\boldsymbol{w}\boldsymbol{w}^\top$ captures shared, rank-one correlation structure across all tasks, and $\boldsymbol{\kappa} \in \mathbb{R}^T_{>0}$ is a vector of strictly positive task-specific variances that allow each task to retain an independent component. This construction guarantees that $\boldsymbol{B}$ is positive semi-definite for any $\boldsymbol{w}$ and $\boldsymbol{\kappa}$, and it spans the full range from strong inter-task correlation (dominant $\boldsymbol{w}\boldsymbol{w}^\top$) to effectively independent tasks (dominant $\mathrm{diag}(\boldsymbol{\kappa})$), so the appropriate degree of information sharing is learned from the data rather than imposed. The prior mean is task-specific, $\mu(\boldsymbol{x}, \tau) = c_\tau$, assigning an independent constant to each task, and the noise is homoscedastic and shared across the tasks of a given model, $\sigma_n^2(\boldsymbol{x}, \tau) = \sigma_n^2$. The complete hyperparameter set for a multitask model is therefore $\boldsymbol{\theta} = \{\sigma_s^2, l_1, l_2, \boldsymbol{w}, \boldsymbol{\kappa}, \sigma_n^2, \{c_\tau\}_{\tau=1}^T\}$, learned jointly by maximizing the log marginal likelihood over all tasks simultaneously.

The mixture model at each point $\boldsymbol{x} = \{P, V\}$ is characterized by $3K - 1 = 11$ parameters per pore property: four log-means $\{\mu_k\}_{k=1}^4$, four log-variances $\{\sigma_k^2\}_{k=1}^4$, and three independent mixture weights $\{w_k\}_{k=1}^3$, all treated as unknown functions of laser power P and scan velocity V.

To satisfy the simplex constraint on the mixture weights, requiring $\sum_{k=1}^K w_k(\boldsymbol{x}) = 1$ and $w_k(\boldsymbol{x}) \geq 0$, the weights are mapped to an unconstrained space prior to GPR modeling using the additive log-ratio (ALR) transform. Specifically, the $K - 1 = 3$ unconstrained variables $z_i(\boldsymbol{x})$ are defined as:

$$z_i(\boldsymbol{x}) = \log \frac{w_i(\boldsymbol{x})}{w_K(\boldsymbol{x})}, \quad i = 1, 2, 3, \tag{5}$$

where w_K serves as the reference category. The ALR transform is a bijection from the $(K-1)$-simplex to $\mathbb{R}^{K-1}$, ensuring that the GPR operates on variables with unbounded real-valued support—consistent with the Gaussian likelihood assumption—while the original weights are exactly recovered via the inverse transform:

$$w_i(\boldsymbol{x}) = \frac{\exp(z_i(\boldsymbol{x}))}{1 + \sum_{j=1}^{K-1} \exp(z_j(\boldsymbol{x}))}, \qquad w_K(\boldsymbol{x}) = \frac{1}{1 + \sum_{j=1}^{K-1} \exp(z_j(\boldsymbol{x}))}. \tag{6}$$

These 11 parameters are grouped into three multitask GPR models, each taking $\boldsymbol{x} = \{P, V\}$ as input:

- Multitask GPR 1 predicts the four log-means $\{\mu_k(\boldsymbol{x})\}_{k=1}^4$ jointly ($T = 4$ tasks), as they are already defined on the real line and require no transformation.
- Multitask GPR 2 predicts the four log-variances via their natural logarithm $\{\log(\sigma_k^2(\boldsymbol{x}))\}_{k=1}^4$ ($T = 4$ tasks), which maps the strictly positive variances to an unbounded real-valued space consistent with the Gaussian likelihood assumption of the Gaussian process.
- Multitask GPR 3 predicts the three ALR-transformed weights $\{z_i(\boldsymbol{x})\}_{i=1}^3$ ($T = 3$ tasks), where the additive log-ratio transform maps the constrained mixture weights to an unconstrained space, as described below.

Since pore properties are modeled separately for sphericity and maximum Feret diameter, this results in six multitask GPR models in total, three per pore property. Within each model, the four (or three, for the weights) mixture components are the tasks, and the LMC kernel of Eq. 3 allows the model to share information across components—for example, exploiting the fact that neighboring lognormal components tend to shift together as the processing regime changes—while still permitting each component to vary independently where the data demand it. The reconstructed mixture weights are guaranteed to be strictly positive and to sum to exactly one at any point in the parameter space, without requiring post hoc normalization.

Active learning parameter space exploration

Active learning with an information-driven acquisition function is used to efficiently explore the AM laser power–scan velocity parameter space $\boldsymbol{x} = \{P, V\} \in \boldsymbol{X} \subset \mathbb{R}^2$, an approach that has emerged in the AM field for characterizing black-box latent functions relating process parameters to functional properties [24, 33–35]. It is a closed-loop strategy that iteratively learns from available data to suggest new experiments by optimizing an acquisition function that determines the most informative experiment to run next. Active learning has been shown to outperform other parameter-space exploration strategies, such as random sampling, grid sampling, genetic algorithms, and Lagrange-relaxation optimization, in applications characterized by low data density [13–16].

Active learning comprises a stochastic estimator of the latent function, here the GPR surrogates of the mixture parameters, together with an acquisition function. The GPR's predictive uncertainties are essential for closed-loop exploration, as they are one of the main inputs to the acquisition function that identifies the next point to test. The procedure builds the dataset in multiple steps: selecting a point to test, performing the experiment, and updating the GPR models. In the first step, points are randomly selected to build the initial GPR models. At each subsequent step, the acquisition function selects the next point, and the GPR models are refit as new data become available.

The acquisition function defines the active-learning objective and determines whether the search emphasizes exploration of the parameter space, exploitation for optimization, or a balance of the two. One of the most widely used acquisition functions is Expected Improvement, which balances exploration and exploitation for global optimization [36]. However, the goal of this work is pure exploration of the parameter space to efficiently characterize the full pore-property distributions as functions of the process parameters. We therefore employ a distribution-level epistemic-uncertainty-based acquisition function that selects the point at which the surrogate is most uncertain about the shape of the predicted property distribution.

Because each morphological property is described by a four-component lognormal mixture whose parameters are predicted by three multitask GPR models (component log-means, component log-variances, and mixture weights), the acquisition criterion is evaluated at the level of the predicted probability density rather than on any single GPR output. At a candidate point $\boldsymbol{x}$, the three GPR models governing a property's mixture parameters are sampled jointly from their epistemic posteriors using the noise-free posterior covariance. This allows epistemic uncertainty only, not aleatoric variability, to drive selection. Each joint sample $s = 1, \ldots, S$ yields a realization $\phi_s(\boldsymbol{x})$ of the mixture parameters defined in Eq. 1, which is mapped through the mixture parameterization to a full lognormal-mixture density $p_s(d \mid \boldsymbol{x}) = \mathcal{P}(d \mid \phi_s(\boldsymbol{x}))$ over the property's physical support d. For instance, sphericity is supported on 400 equally spaced points in the range of [0.45, 1], and for maximum Feret diameter [0.01, 100] μm. The uncertainty U for a property q is the probability-mass-weighted integral of the pointwise ensemble variance of these densities, characterized by:

$$U_q(\boldsymbol{x}) \;=\; \int \mathrm{Var}_s\big[p_s(d \mid \boldsymbol{x})\big]\, \bar{p}(d \mid \boldsymbol{x})\, \mathrm{d}d, \qquad \bar{p}(d \mid \boldsymbol{x}) = \frac{1}{S}\sum_{s=1}^{S} p_s(d \mid \boldsymbol{x}), \tag{7}$$

where $\mathrm{Var}_s[\cdot]$ denotes the variance across the posterior ensemble at each point of the support, and $\bar{p}$ is the posterior-mean density. This weighting captures disagreement about where the predicted distribution's probability mass actually lies, rather than in low-density regions of the support. The two per-property uncertainties are each normalized by a precomputed scale c_q, the mean of U_q over a coarse grid of the design space, and summed to form the acquisition score:

$$a(\boldsymbol{x}) \;=\; \sum_{q \in \{\mathrm{diam},\, \mathrm{sph}\}} \frac{U_q(\boldsymbol{x})}{c_q}, \tag{8}$$

and the next experiment is chosen as $\boldsymbol{x}^* = \arg\max_{\boldsymbol{x} \in \boldsymbol{X}} a(\boldsymbol{x})$, optimized by differential evolution. Because c_q is computed via the same integral as $U_q(x)$ (Eq. 7), merely averaged over the design space rather than evaluated at a point, the ratio $U_q(x)/c_q$ is dimensionless regardless of the physical units or support range of property q, allowing the two per-property uncertainty scores to be combined

Algorithm 1 Distribution-level epistemic-uncertainty active learning for pore property exploration

Require: Normalized design space $\boldsymbol{X} = [0,1]^2$; initial random design size n_0; Ground Truth (GT) providing mixture-parameter observations; number of active learning steps n_{total}; Monte Carlo sample count S; per-property supports $\{D_q\}$

Ensure: Explored dataset $\mathcal{D}$; fitted surrogate GPRs

$\boldsymbol{X}_{\text{obs}} \leftarrow n_0$ random points (fixed per-trial seed)
$\boldsymbol{Y}_{\text{obs}} \leftarrow \text{GT}(\boldsymbol{X}_{\text{obs}})$ ▷ log-means, log-vars, ALR weights per property
for step $= 1$ **to** n_{total} **do**
    Fit surrogates: train the six GPRs on $(\boldsymbol{X}_{\text{obs}}, \boldsymbol{Y}_{\text{obs}})$ by MLE
    for each property $q \in \{\text{diam}, \text{sph}\}$ **do** ▷ normalization scales
        $c_q \leftarrow$ mean of $U_q(\boldsymbol{x})$ over a coarse grid of $\boldsymbol{X}$
    end for
    function $a(\boldsymbol{x})$ ▷ acquisition score
        total $\leftarrow 0$
        for each property $q \in \{\text{diam}, \text{sph}\}$ **do**
            Draw S joint posterior samples of (means, log-vars, weights) at $\boldsymbol{x}$ using the *noise-free* posterior covariance ▷ epistemic only
            Map each sample s to a lognormal-mixture density $p_s(\cdot)$ on D_q
            $\bar{p} \leftarrow \frac{1}{S}\sum_s p_s$; $v \leftarrow \text{Var}_s\, p_s$
            $U_q \leftarrow \int v(d)\,\bar{p}(d)\,\mathrm{d}d$ ▷ trapezoidal rule
            total $\leftarrow$ total $+ U_q / c_q$
        end for
        return total
    end function
    $\boldsymbol{x}^* \leftarrow \arg\max_{\boldsymbol{x} \in \boldsymbol{X}} a(\boldsymbol{x})$ ▷ via differential evolution
    $\boldsymbol{y}^* \leftarrow \text{GT}(\boldsymbol{x}^*)$
    $\boldsymbol{X}_{\text{obs}} \leftarrow \boldsymbol{X}_{\text{obs}} \cup \{\boldsymbol{x}^*\}$; $\boldsymbol{Y}_{\text{obs}} \leftarrow \boldsymbol{Y}_{\text{obs}} \cup \{\boldsymbol{y}^*\}$
    Record distribution metrics (W_1, KL, LPD) against ground truth
end for
return $(\boldsymbol{X}_{\text{obs}}, \boldsymbol{Y}_{\text{obs}})$, fitted GPRs

additively in Eq. 8 without unit mismatch. Both properties are included because each new experiment simultaneously characterizes both distributions. The integrals over the support and the ensemble variance are estimated numerically from the S Monte Carlo posterior samples. Each acquisition evaluation uses $S = 800$ Monte Carlo posterior samples; the normalization scales c_q are precomputed with $S = 400$ samples over a 20×20 grid of the design space. Algorithm 1 illustrates the pseudocode of the acquisition function used in this work.

Stopping criterion: marginal KL divergence between successive posteriors

The acquisition function of Eq. 8 identifies the most informative next experiment but does not, by itself, indicate when the experimental campaign can be terminated. In this work, we assess convergence of the predicted pore-property distributions against the ground-truth surrogate using the distribution-level metrics in the Results section; however, in a physical, non-simulated campaign, no such ground truth is available, and stopping decisions must instead be made based on information intrinsic to the surrogate itself. We therefore introduce a budget-free stopping diagnostic based on the relative information gain between the surrogate's predicted pore-property distribution at successive active-learning steps.

At step t, the posterior means of the six multitask GPR models are evaluated at a fixed set of $N = 100$ reference points $\{\mathbf{x}_i\}_{i=1}^{N}$, generated using the same Latin hypercube design used for the ground-truth comparison in the Results section (Figure S3). At each reference point, the posterior-mean mixture parameters $\hat{\phi}_t^q(\boldsymbol{x}_i)$—comprising the four log-means, four log-variances, and four weights

(recovered from the three ALR-transformed variables via Eq. 6), for property $q \in \{\mathrm{diam}, \mathrm{sph}\}$—are substituted into the lognormal-mixture form of Eq. 1 to obtain a single deterministic density $\mathcal{P}(d \mid \hat{\boldsymbol{\phi}}_t^q(\mathbf{x}_i))$ over the property's support. These N densities are averaged to obtain a single marginal mixture density summarizing the surrogate's current belief about property q across the entire parameter space:

$$\hat{p}_t^q(d) \;=\; \frac{1}{N}\sum_{i=1}^{N} \mathcal{P}\Big(d \mid \hat{\boldsymbol{\phi}}_t^q(\boldsymbol{x}_i)\Big)\,. \tag{9}$$

Here, $\hat{\boldsymbol{\phi}}_t^q(\boldsymbol{x}_i)$ denotes the GPR posterior-mean estimate, at active-learning step t, of the mixture parameters $\boldsymbol{\phi}^q(\boldsymbol{x}_i)$ defined in Eq. 1 (the hat indicating an estimated, rather than true, quantity). Unlike the epistemic-uncertainty acquisition score of Eq. 7, which requires S Monte Carlo draws from the joint posterior at each candidate point, Eq. 9 uses only the posterior *mean* prediction and therefore requires no additional sampling; it is computed with the same routine used to construct the predicted mixture in the ground-truth comparison metrics, adding negligible overhead to each active-learning step.

The step-wise marginal information gain added by step t is quantified using the marginal Kullback–Leibler (KL) divergence between successive posterior predictive states:

$$I^q_{\mathrm{marginal},t} = D_{\mathrm{KL}}\big(\hat{p}^q_{t-1} \,\|\, \hat{p}^q_t\big) = \int \hat{p}^q_{t-1}(d)\log\left(\frac{\hat{p}^q_{t-1}(d)}{\hat{p}^q_t(d)}\right)\mathrm{d}d, \tag{10}$$

evaluated independently for sphericity and maximum Feret diameter. This direction weights the divergence by where the previous posterior placed probability mass, so that $I^q_{\mathrm{marginal},t}$ is large precisely when the surrogate's updated belief has shifted away from a region it was previously confident about, and small when the new posterior remains consistent with the old one in the regions that previously carried most of the probability mass. Because Eq. 10 compares the surrogate only against its own previous state, it requires no ground truth and applies directly to physical, closed-loop LPBF campaigns.

The cumulative information accumulated up to step t is computed as the running sum of step-wise gains:

$$I^q_{\mathrm{cumulative},t} = \sum_{i=1}^{t} I^q_{\mathrm{marginal},i}. \tag{11}$$

A sustained decrease in $I^q_{\mathrm{marginal},t}$ relative to the total accumulated knowledge indicates that newly acquired experiments are producing diminishing changes to the surrogate's characterization of the pore-property distribution across the parameter space. To establish an objective, threshold-based termination criterion, the active learning process evaluates the ratio of marginal step gain to total cumulative information gained. The campaign is triggered to stop at the first step t^* where the single-step marginal information gain drops below 2.5% of the cumulative information acquired up to that point:

$$I^q_{\mathrm{marginal},t^*} < 0.025 \times I^q_{\mathrm{cumulative},t^*}. \tag{12}$$

We examine the empirical behavior of this diagnostic, and its relationship to the ground-truth-based accuracy metrics of Figure 5, in the Results (Figure 6). Note that $I^q_{\mathrm{marginal},t}$ is undefined at the first step of a campaign, since no previous posterior $\hat{p}^q_{t-1}$ exists for comparison; the cumulative information gain $I^q_{\mathrm{cumulative},t}$ is therefore only defined from the second step onward.

Declarations

Acknowledgments

M.B.A. and M.M.N. acknowledge the Center of Advanced Mathematics for Energy Research applications (CAMERA), funded by the U.S. Department of Energy, Office of Advanced Scientific Computing Research and Basic Energy Sciences under contract No. DE-AC02-05CH11231.

Supplementary Information Availability

Supplementary information is attached to this manuscript.

Data and Code Availability Statement

All used code and data will be made available upon publication.

Conflict of interest

The authors declare no conflicts of interest.

Author Contributions

M.B.A. and N.K. conceptualized and supervised the work. T.U.A. performed the experiments, μ-CT characterization, and data collection. M.B.A. and M.M.N. developed the stochastic representation of the pore property data and designed the distribution-level acquisition function. M.B.A. conceptualized and developed the stopping criterion and wrote the first draft. All authors reviewed the manuscript.

References

[1] Zhou, L., Miller, J., Vezza, J., Mayster, M., Raffay, M., Justice, Q., Al Tamimi, Z., Hansotte, G., Sunkara, L.D., Bernat, J.: Additive manufacturing: a comprehensive review. Sensors **24**(9), 2668 (2024)

[2] Raisa, F.K., Singh, R.K., Bettencourt, C.J., Berke, R.B., Kouraytem, N.: Integrity of welding of laser powder bed fusion haynes 282 alloy under creep conditions for concentrated solar power systems. JOM, 1–11 (2026)

[3] Mostafaei, A., Zhao, C., He, Y., Ghiaasiaan, S.R., Shi, B., Shao, S., Shamsaei, N., Wu, Z., Kouraytem, N., Sun, T., *et al.*: Defects and anomalies in powder bed fusion metal additive manufacturing. Current Opinion in Solid State and Materials Science **26**(2), 100974 (2022)

[4] DebRoy, T., Wei, H.L., Zuback, J.S., Mukherjee, T., Elmer, J.W., Milewski, J.O., Beese, A.M., Wilson-Heid, A., De, A., Zhang, W.: Additive manufacturing of metallic components–process, structure and properties. Progress in Materials Science **92**, 112–224 (2018) https://doi.org/10.1016/j.pmatsci.2017.10.001

[5] Snow, Z., Diehl, B., Reutzel, E.W., Nassar, A.: Toward in-situ flaw detection in laser powder bed fusion additive manufacturing through feedforward training of neural networks. Materials & Design **183**, 108140 (2019) https://doi.org/10.1016/j.matdes.2019.108140

[6] Anwar, T.U., Merighe, P., Kancharla, R.R., Kombaiah, B., Kouraytem, N.: Influence of process parameter and build rate variations on defect formation in laser powder bed fusion ss316l. Materials **18**(2), 435 (2025)

[7] Gordon, J.V., Narra, S.P., Cunningham, R.W., Liu, H., Chen, H., Suter, R.M., Beuth, J.L., Rollett, A.D.: Defect structure process maps for laser powder bed fusion additive manufacturing. Additive Manufacturing **36**, 101552 (2020)

[8] Holm, E.A.: In defense of the black box. Science **364**(6435), 26–27 (2019)

[9] Kouraytem, N., Li, X., Tan, W., Kappes, B., Spear, A.D.: Modeling process–structure–property relationships in metal additive manufacturing: a review on physics-driven versus data-driven approaches. Journal of Physics: Materials **4**(3), 032002 (2021)

[10] Liu, Q., Wu, H., Paul, M.J., He, P., Peng, Z., Gludovatz, B., Kruzic, J.J., Wang, C.H., Li, X.: Machine-learning assisted laser powder bed fusion process optimization for alsi10mg: New microstructure description indices and fracture mechanisms. Acta Materialia **201**, 316–328 (2020)

[11] Tapia, G., Elwany, A.H., Sang, H.: Prediction of porosity in metal-based additive manufacturing using spatial gaussian process models. Additive Manufacturing **12**, 282–290 (2016)

[12] Tapia, G., Khairallah, S., Matthews, M., King, W.E., Elwany, A.: Gaussian process-based surrogate modeling framework for process planning in laser powder-bed fusion additive manufacturing of 316l stainless steel. The International Journal of Advanced Manufacturing Technology **94**(9), 3591–3603 (2018)

[13] Agarwal, G., Doan, H.A., Robertson, L.A., Zhang, L., Assary, R.S.: Discovery of energy storage molecular materials using quantum chemistry-guided multiobjective bayesian optimization. Chemistry of Materials **33**(20), 8133–8144 (2021)

[14] Nikolaidis, P., Chatzis, S.: Gaussian process-based bayesian optimization for data-driven unit commitment. International Journal of Electrical Power & Energy Systems **130**, 106930 (2021)

[15] Harada, M., Takeda, H., Suzuki, S., Nakano, K., Tanibata, N., Nakayama, M., Karasuyama, M., Takeuchi, I.: Bayesian-optimization-guided experimental search of nasicon-type solid electrolytes for all-solid-state li-ion batteries. Journal of Materials Chemistry A **8**(30), 15103–15109 (2020)

[16] Sorourifar, F., Choksi, N., Paulson, J.A.: Computationally efficient integrated design and predictive control of flexible energy systems using multi-fidelity simulation-based bayesian optimization. Optimal Control Applications and Methods **44**(2), 549–576 (2023)

[17] Sanaei, N., Fatemi, A.: Defects in additive manufactured metals and their effect on fatigue performance: A state-of-the-art review. Progress in Materials Science **117**, 100724 (2021)

[18] Romano, S., Brandão, A., Gumpinger, J., Gschweitl, M., Beretta, S.: Qualification of am parts: Extreme value statistics applied to tomographic measurements. Materials & Design **131**, 32–48 (2017)

[19] Beretta, S., Romano, S.: A comparison of fatigue strength sensitivity to defects for materials manufactured by am or traditional processes. International Journal of Fatigue **94**, 178–191 (2017)

[20] Cerezo, P.M., Aguilera, J.A., Garcia-Gonzalez, A., Lopez-Crespo, P.: Tomography of laser powder bed fusion maraging steel. Materials **17**(4), 891 (2024)

[21] Peng, X., Wu, S., Qian, W., Bao, J., Hu, Y., Zhan, Z., Guo, G., Withers, P.J.: The potency of defects on fatigue of additively manufactured metals. International Journal of Mechanical Sciences **221**, 107185 (2022)

[22] Ogoke, O.F., Johnson, K., Glinsky, M., Laursen, C., Kramer, S., Farimani, A.B.: Deep-learned generators of porosity distributions produced during metal additive manufacturing. Additive Manufacturing **60**, 103250 (2022)

[23] Anwar, T.U., Higdon, R., Seo, J., Rollett, A.D., Kouraytem, N.: A defect criticality index for refining the process windows of ss316l fabricated by laser powder bed fusion: Insights from μ-ct based defect characterization (2026). Manuscript under review

[24] Alghalayini, M.B., Paredis, C.J., Abdeljawad, F.: Sequential design optimization of high-variability additive manufacturing processes using gaussian process regression. Journal of Manufacturing Processes **158**, 294–307 (2026)

[25] Nudelis, N., Mayr, P.: A novel classification method for pores in laser powder bed fusion. Metals **11**(12), 1912 (2021)

[26] Mishurova, T., Evsevleev, S., Piault, P., King, A., Henry, L., Bruno, G.: Understanding the hot isostatic pressing effectiveness of laser powder bed fusion ti-6al-4v by in-situ x-ray imaging and diffraction experiments. Scientific reports **13**(1), 18433 (2023)

[27] Comet Technologies Canada Inc.: Dragonfly 2022.2, Montreal, Canada. [Computer software] (2022). https://dragonfly.comet.tech/

[28] Micchelli, C.A., Xu, Y., Zhang, H.: Universal kernels. Journal of Machine Learning Research **7**(12) (2006)

[29] Seeger, M.W., Kakade, S.M., Foster, D.P.: Information consistency of nonparametric gaussian process methods. IEEE Transactions on Information Theory **54**(5), 2376–2382 (2008)

[30] Vaart, A.W., Zanten, J.H.: Adaptive bayesian estimation using a gaussian random field with inverse gamma bandwidth. The Annals of Statistics **37**(5B), 2655–2675 (2009) https://doi.org/

10.1214/08-AOS678

[31] Alghalayini, M.B., Collins-Wildman, D., Higa, K., Guevara, A., Battaglia, V., Noack, M.M., Harris, S.J.: Machine-learning-based efficient parameter space exploration for energy storage systems. Cell Reports Physical Science **6**(4) (2025)

[32] Alghalayini, M.B., Harris, S.J., Noack, M.M.: Early prediction of the failure probability distribution for energy-storage driven by domain-knowledge-informed machine learning. Cell Reports Physical Science **6**(6) (2025)

[33] Aqib, M., Ravikiran, K., Li, L., Prasad, V.: A multi-fidelity active learning framework for accelerated alloy design. Materials & Design, 115520 (2026)

[34] Nasrin, T., Pourali, M., Pourkamali-Anaraki, F., Peterson, A.M.: Active learning for prediction of tensile properties for material extrusion additive manufacturing. Scientific reports **13**(1), 11460 (2023)

[35] Mojumder, S., Gan, Z., Li, Y., Al Amin, A., Liu, W.K.: Linking process parameters with lack-of-fusion porosity for laser powder bed fusion metal additive manufacturing. Additive Manufacturing **68**, 103500 (2023)

[36] Jones, D.R., Schonlau, M., Welch, W.J.: Efficient global optimization of expensive black-box functions. Journal of Global optimization **13**(4), 455–492 (1998)